Acta Materialia 212 (2021) 116914

Contents lists available at ScienceDirect

Acta Materialia

journal homepage: www.elsevier.com/locate/actamat

Surface-dependent stress-corrosion cracking in Ni-rich layered oxide cathodes

Weifeng Wei[a,1], Zhengping Ding[b,1], Cheng Chen[a,1], Cheng Yang[a], Bo Han[a], Lei Xiao[a], Chaoping Liang[a,*], Peng Gao[b,*], Kyeongjae Cho[c]

[a] State Key Laboratory of Powder Metallurgy, Central South University, Changsha, Hunan 410083, People's Republic of China
[b] International Center for Quantum Materials & Electron Microscopy Laboratory, School of Physics, Peking University, Beijing, 100871, People's Republic of China
[c] Materials Science & Engineering Department, The University of Texas at Dallas, Richardson, TX 75080, United States

ARTICLE INFO

Article history:
Received 5 August 2020
Revised 12 April 2021
Accepted 15 April 2021
Available online 22 April 2021

Keywords:
Li-ion battery
Electrochemical characterization
Oxides
Cracking
Corrosion

ABSTRACT

Structural degradation is the principal driving force for rapid voltage decay and capacity fading of Ni-rich layered oxide (NLO) cathode materials upon cycling, but its working mechanism is not yet fully elucidated. In this work, multi-scale electron microscopy/spectroscopy techniques and theoretical calculations are applied on both polycrystalline and single-crystal NLOs. We discover that both the intergranular and intragranular cracks initiate along polar (001) basal plane, while surface structure evolution and transition metal dissolution occur on nonpolar (104) fresh surface. A new chain stress corrosion mechanism from anisotropic elastic (001) tensile deformation, microcrack generation, nonpolar surface reconstruction, HF attack to metal dissolution is proposed to paint the full picture of the structural degradation of NLOs. This surface-dependent stress-corrosion coupling effect indicates that severe intergranular cracking that accumulates within the polycrystalline NLO aggregates accounts mostly for the fast voltage decay and capacity fading, whereas minor intragranular cracking and less surface damage lead to substantial improvements on cyclability and reversible capacity of single-crystal NLOs. The surface-dependent stress-corrosion cracking in both polycrystalline and single-crystal NLOs provides grain-boundary engineering clues on designing new cathode materials with high energy density and long cycle life.

1. Introduction

Nickel-rich layered oxide (NLO) cathodes have been considered as a class of major material candidates for next generation lithium ion batteries (LIBs) due to their high reversible capacities (~180–220 mA h g^{-1}), high rate capability, and low cost [1–3]. To take full advantage of lithium utilization, it is desirable to raise the Ni content of the NLO cathodes toward $LiNi_{0.8}Co_{0.1}Mn_{0.1}O_2$ (NCM811) and LiNi0.8Co0.15Al0.05O_2 (NCA) or even higher, and/or to charge the NLO cathodes to a voltage above 4.5 V *vs.* Li/Li^+ [4]. However, excessive delithiation from these NLO cathodes usually degrades the structural integrity and leads to rapid performance decay. Many degradation mechanisms have been proposed in the literature, such as surface reconstruction [5], surface side reactions, cation dissolution into the electrolyte [6], and crack propagation (e.g., intergranular cracking [7–9], and intragranular cracking [10,11]).

A huge endeavor has been undertaken to reinforce those weakest link in the fully lithium utilization in NLO cathodes. Diverse approaches, including elemental doping [12], gradient structure [13], core-shell structure [14], surface coating [15], and hierarchical microstructures [16], have been explored to suppress the degradation of polycrystalline NLOs. For instance, the phase transformation induced by cation mixing and surface deterioration processes can be significantly suppressed through the elemental doping and surface treatments [12–17]. However, severe micro-crack propagation within the polycrystalline aggregates remains challenging in wide-ranging NLO cathodes with Ni contents over 0.8 [18]. The fundamental origin of intergranular cracking along the boundaries between primary particles is attributed to the drastic anisotropic variations of lattice parameters, which are generated by various states of charge (SOC) in randomly distributed primary particles at deep charged state [4]. The crack propagation reduces the electric connectivity of adjacent primary particles, resulting in inhomogeneous reaction kinetics between cracked and intact areas. The re-

* Corresponding authors.
E-mail addresses: cpliang@csu.edu.cn (C. Liang), p-gao@pku.edu.cn (P. Gao).
[1] These authors contributed equally to the work.

https://doi.org/10.1016/j.actamat.2021.116914
1359-6454/

action inhomogeneity further raises the variation in the Li composition in primary particles, and in turn, deteriorates the lattice anisotropy and leads to extensive crack propagation within the polycrystalline aggregates upon cycling.

Recently, single-crystal NLOs have gained increasing research attentions in the LIBs for electric vehicles, due to their improved long-term cycling performance [19–22]. In comparison to the polycrystalline counterparts, single-crystal NLOs could preserve the original particle shape during cycling as a result of no intergranular cracking. However, without short-circuit diffusion pathway along grain boundaries, single-crystal NLOs present higher voltage polarization, poorer rate performance and lower initial capacity [23]. As they are usually synthesized at higher temperatures, single-crystal NLOs also have higher levels of cation mixing and thicker surface reconstruction layers, which may cause severer structural degradation at higher voltages [23,24]. Besides, reduced particle size are observed after cycling by operando X-ray spectroscopy imaging and nano-tomography, indicating TM dissolution on the particle surface [23]. Thus, similar modifications are proposed to solve these shortcomings of single-crystal NLOs [20,21,23]. Nevertheless, the electrochemical difference between single-crystal and polycrystalline NLOs has yet to be well understood, and those modification methods need to be elucidated and reevaluated based on the electrochemical signatures of single-crystal NLOs.

In this work, a systematic study on structural degradation behavior of polycrystalline (N83) and single-crystal Ni-rich (S83) $LiNi_{0.83}Co_{0.1}Mn_{0.07}O_2$ materials is performed using electron microscopy and affiliated spectroscopies at multi-length scale. The similarities and differences of cracking behavior between single-crystal and polycrystalline NLO cathode materials are examined. A surface-dependent stress-corrosion mechanism is proposed to understand severe intergranular cracking with fast voltage decay and capacity fading in polycrystalline NLO aggregates, and substantial enhancements on cycle life and reversible capacity in single-crystal NLO material. Based on the stress-corrosion mechanism, grain-boundary engineering for NLOs is proposed and discussed in detailed, providing guidance to design better cathode materials for advanced batteries.

2. Experimental procedures

2.1. Materials preparation

$[Ni_{0.83}Co_{0.1}Mn_{0.07}](OH)_2$ precursor was produced using a co-precipitation method. Specifically, a 2.0 M aqueous solution of $NiSO_4{\cdot}6H_2O$, $CoSO_4{\cdot}7H_2O$, and $MnSO_4{\cdot}H_2O$, with the desired Ni:Co:Mn ratios, as the starting materials was added into a 5L continuously stirring tank reactor (CSTR) using a peristaltic pump. Meanwhile, a 0.2 M NaOH solution as the precipitation agent and a 0.24 M NH_4OH solution as the chelation agent were also slowly pumped into the reactor. The co-precipitation parameters such as stirring rate (800 rpm), solution temperature (55 °C) and pH (11.0) were carefully regulated. Collected precursors were vacuum filtered, washed and dried at 110 °C over 12 h. To obtain single-crystal NLO material, the as prepared precursors with stoichiometric $LiOH{\cdot}H_2O$ (Li/TM = 1.07) were calcined at 900 °C for 12 h under pure oxygen atmosphere and cooled down slowly in the furnace. The as-calcinated $LiNi_{0.83}Co_{0.1}Mn_{0.07}O_2$ single-crystal NLO material was named S83. For comparison, $[Ni_{0.83}Co_{0.1}Mn_{0.07}](OH)_2$ precursor was selected to prepared the polycrystalline NLO aggregates at 800 °C for 20 h under pure oxygen atmosphere, and named as N83.

2.2. Materials characterization

The chemical composition of the as-prepared single-crystal and polycrystalline cathode materials was estimated using inductively coupled plasma-atomic emission spectrometry (ICP-AES). Crystallographic structure was evaluated using X-ray diffraction (XRD, Bruker D8 Advance) equipped with Cu Kα radiation source in the scan range of 10-80° and Rietveld refinement of the XRD data was accomplished by General Structure Analysis System (GSAS) software [25]. The plan-view and cross-sectional view morphology was characterized using field-emission scanning electron microscopy (FESEM, FEG250, FEI QUANTA). Cross-sectional samples analyzed by FESEM and scanning transmission electron microscopy (STEM) were sliced and thinned using traditional lift-out focus ion beam (FIB, FEI Helios NanoLab G3) process at 2 to 30 kV. High-resolution TEM images and STEM HAADF images were carried out on an aberration-corrected FEI (Titan Cubed Themis G2) equipped with an X-FEG gun at 300 kV. The beam current was ~50 pA, the convergence semiangle was 30 mrad, and a collection semi-angle snap was 80–379 mrad. STEM-EDX line scan were acquired at a beam current of ~100 pA and counts ranging from 1k cps to 3k cps for ~15 min with a Bruker Super-X EDS four-detector. All electron energy loss spectroscopy (EELS) spectra were acquired on a Gatan Enfinium ER 977 system. The EELS data was acquired at the collection semi-angle of 5.9 mrad, the convergence semi-angle of 25 mrad and a dispersion of 0.25 eV/ch. The EELS date is processed by Digital Micrograph software (Gatan, USA).

2.3. Electrochemical testing

To manufacture the NLO cathodes, a slurry of the active materials, polyvinylidene fluoride (PVDF) and acetylene black in a weight ratio of 8:1:1 in N-methyl-2-pyrrolidone (NMP) was pasted onto Al foil and dried at 120 °C for 12 h in a vacuum oven. Then the coated foil was punched into circular pieces with a diameter of 1.2 cm and the corresponding active material loading was around 1.8 to 2 mg/cm^2. CR2016 coin-type half-cells consisting of an as-prepared cathode, a Li metal anode, a Celgard 2400 separator and 1 M $LiPF_6$ in EC-EMC-DEC (1:1:1 by weight) electrolyte solution were assembled in an Ar-filled glove box. Electrochemical tests of the as-assembled coin-cells were conducted using a battery testing system (LANHE CT2001A, Wuhan LAND Electronics Co., P. R. China) at 2.8–4.3 V (or 4.5 V) at different current densities. Cyclic voltammetry (CV) data were collected at a scan rate of 0.1 mV/s on a Princeton PARSTAT 4000 (AMETEK Co. Ltd.) workstation. Electrochemical impedance spectroscopy (EIS) was carried out using a Princeton PARSTAT 4000 in a frequency range from 10 mHz to 100 kHz with an AC amplitude of 5 mV. The chemical composition of the cycled electrolyte was estimated through inductively coupled plasma optical emission spectroscopy (ICP-OES). The sample for ICP-OES was prepared by disassembling the coin cell in the Ar-filled glove box and washing out the electrolyte in propylene carbonate (PC).

2.4. Theoretical calculations

The corrosion reaction of delithiated NLO surface and electrolyte was derived by a thorough search of all possible reaction pathways. The surface phase transformation of Ni-rich $LiNi_{0.83}Co_{0.1}Mn_{0.07}O_2$ materials from layered to spinel or layered to rocksalt with the assistance of the combustion of solvent (EC) was calculated based on the first principle calculation data from one of the authors published work [26]. The further reaction between surface reconstruction layers (after phase transformation) and hydrofluoric acid (HF) was constructed by considering all possible metal fluorides (from the Materials Project website) as reaction products and only selecting the reaction with the lowest reaction enthalpy (based on the total energy from the Materials Project website) [27]. Without further specification, the calculated reaction enthalpy is at the ground state (0 K).

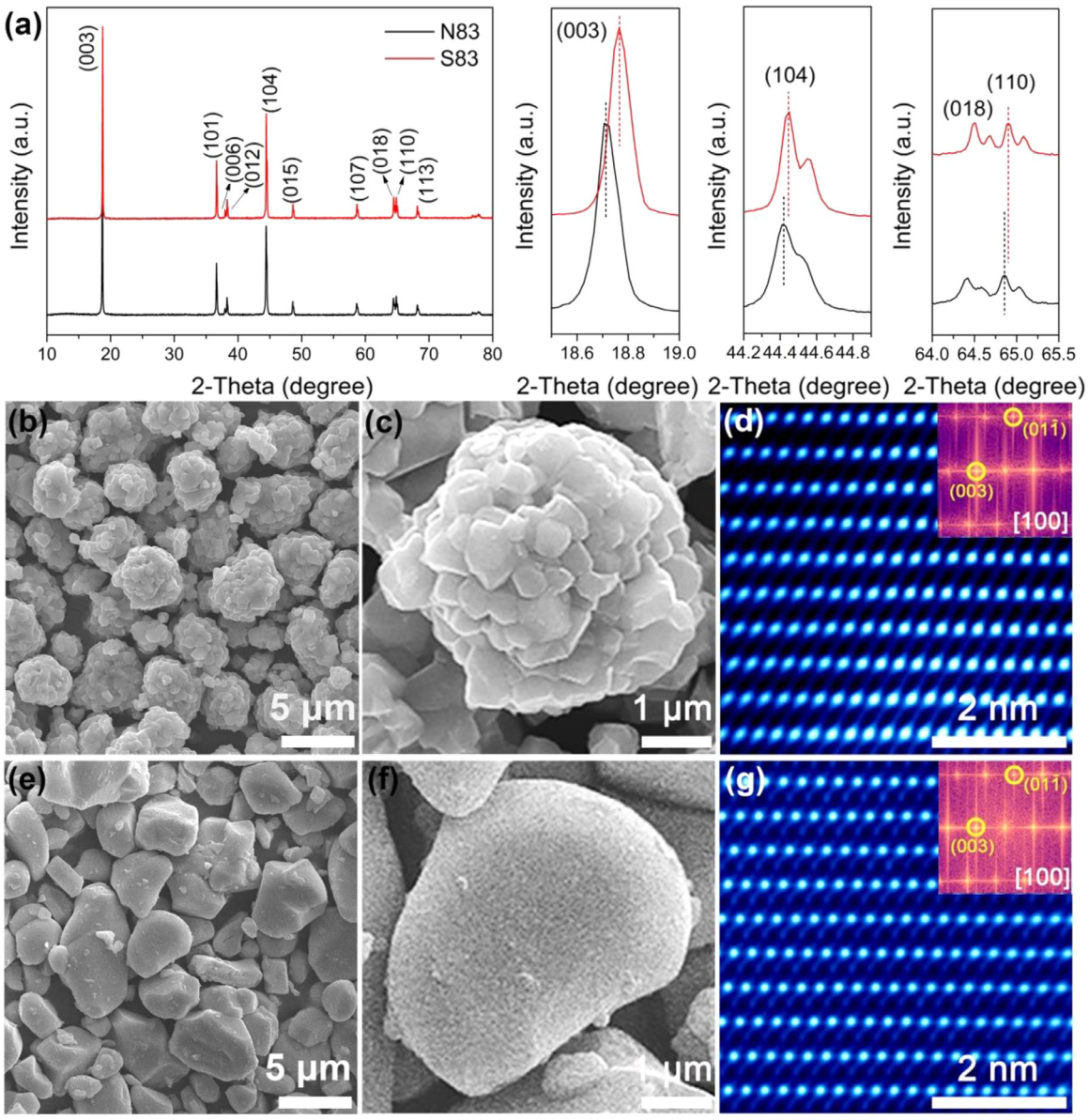

Fig. 1. Structure of N83 and S83 materials. (a) XRD patterns of the N83 and S83 materials. Corresponding enlarged views for the (003), (104) and (110) peaks of the XRD patterns showing peak shifts. (b-d) SEM morphology, atomic-resolution HAADF-STEM image and fast Fourier transformed (FFT) pattern of the N83 material. (e-g) SEM morphology, atomic-resolution HAADF-STEM image and fast Fourier transformed (FFT) pattern of the S83 material.

3. Results and discussion

3.1. Bulk structure and electrochemical properties

The polycrystalline (N83) and single-crystal (S83) Ni-rich $LiNi_{0.83}Co_{0.1}Mn_{0.07}O_2$ materials were synthesized by well controlled co-precipitation method. The as-prepared N83 and S83 have comparable particle properties, such as similar particle size, surface area, and tap density. A layered α-$NaFeO_2$ structure with $R\bar{3}m$ space group was identified for these two materials by powder X-ray diffraction (PXRD) (Fig. 1a) and TEM (Fig. 1d g, and S2 of Supplementary material). The clear split of the (018)/(110) peaks and sharper (014)/(018)/(110) peaks indicate that S83 material exhibits a higher degree of crystallinity than N83 material. Rietveld refinement of XRD patterns (Fig. S1 and Table S1) shows a slight lattice shrinkage in both c and a axes. The slight lattice shrinkage was caused by the increased Li/Ni disorder degree [28] which originates from the excess evaporation of Li source at a higher calcinating temperature of 900 °C (Table S2) [29,30]. The SEM morphology of the polycrystalline N83 and single-crystal S83 materials (Fig. 1b-g) shows that N83 is comprised of numerous secondary particles with a diameter of about 3 to 5 μm (Fig. 1b). Each secondary particle is a spherical agglomerate of equiaxed, densely packed primary particles (average 500 nm) (Fig. 1c). In contrast, S83 material is consisted of micro-scale single-crystal particles (~5 μm) with relatively smooth surface (Fig. 1e-f). The cross-section images of N83 and S83 (Fig. 3) particles show typical polycrystalline and single crystalline features, respectively. Besides, we found S83 particle has a thin surface reconstruction layer as compared with the N83 counterpart (Fig. S3), which is line with the increased Li/Ni disorder degree and the experimental observation in the literature [24].

The electrochemical properties of the polycrystalline N83 and single-crystal S83 materials were compared with galvanostatic charge-discharge and cyclic voltammetry (CV) testing at 30 °C. The initial charge-discharge curves (Fig. 2a, 0.1 C from 2.8 to 4.3 V) show that N83 has a higher initial discharge capacity

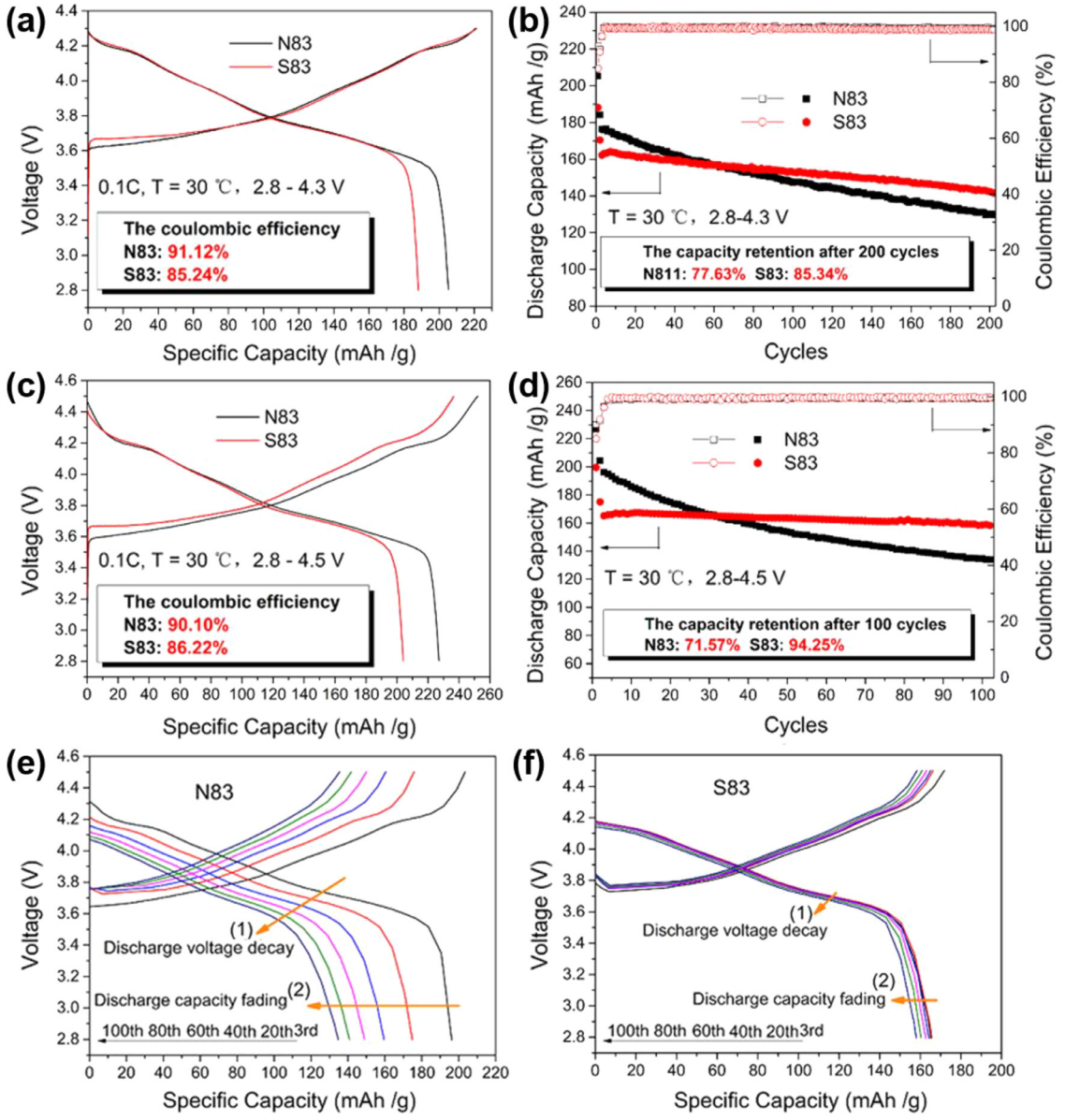

Fig. 2. Electrochemical performance of the N83 and S83 materials. (a) Initial charge–discharge profiles of the N83 and S83 materials tested at a rate of 0.1 C (1 C = 200 mA g^{-1}) between 2.8 and 4.3 V. (b) Cycling performance between 2.8–4.3 V. (c) Initial charge-discharge profiles of both samples tested at a rate of 0.1 C between 2.8 and 4.5 V. (d) Cycling performance between 2.8 and 4.5 V. Galvanic discharge profiles of (e) N83 and (f) S83 materials at a rate of 2 C between 2.8 and 4.5 V.

(205 mAh/g) and Coulombic efficiency (91.12%) than S83 (188 mAh/g and 85.24%). This inferior electrochemical kinetics of S83 material could be attributed to the longer diffusion pathways through micron-scale single-crystal particles and the insulating surface reconstruction layer formed at higher annealing temperature [19,20,23]. However, improved cycling performance is observed in the S83 material (Fig. 2c-d), showing a high-capacity retention over 85% after 200 cycles between 2.8 and 4.3 V and 94.2% after 100 cycles between 2.8 and 4.5 V. The average voltage (Fig. S4), calculated by the result of integral energy on galvanostatic discharge curve divided by discharge capacity (Eq. (1)) in reference 32) [31,32], keeps almost constant for S83 materials, while decreases fast for N83 materials during cycling between 2.8 and 4.5 V. The charge-discharge voltage profiles, compared in Fig. 2e-f, show that S83 material experiences a smaller discharge voltage decay and slower capacity fading in comparison to N83 material.

The structural evolution of polycrystalline N83 and single-crystal S83 particles during cycling was revealed by SEM. The cross-sectioned morphology (Fig. 3) of N83 and S83 particles before and after different cycles shows that polycrystalline aggregates of N83 are pulverized through severe intergranular cracking, while S83 particles keep the initial shape with minor intragranular cracking on the surface and within the grain. The difference in the crack generation and propagation between polycrystalline and single-crystal particles originates from the grain boundary structure. In polycrystalline aggregates there are huge grain boundary areas which provide a lot of crack tips, while single-crystal particle, serves as an extreme example, has almost no grain boundary and thus is immune to intergranular cracking.

3.2. Atomic-resolution characterization of surface and crack tip

To probe the structural and chemical variations along the intergranular and intragranular cracks, HAADF-STEM imaging, energy dispersive spectroscopy (EDS) and electron energy loss spectroscopy (EELS) analyses were carried out on the FIB-sectioned,

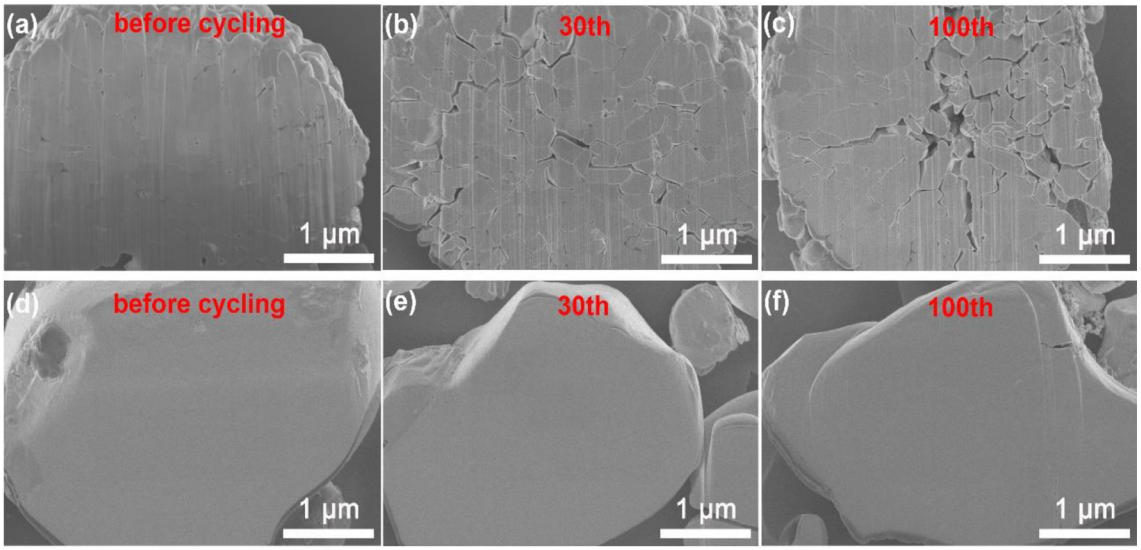

Fig. 3. SEM images of the cross-sectioned, cycled N83 aggregates and S83 single crystal particles after different cycles between 2.8–4.5 V. (a, d) before cycling, (b, e) 30th and (c, f) 100th cycles.

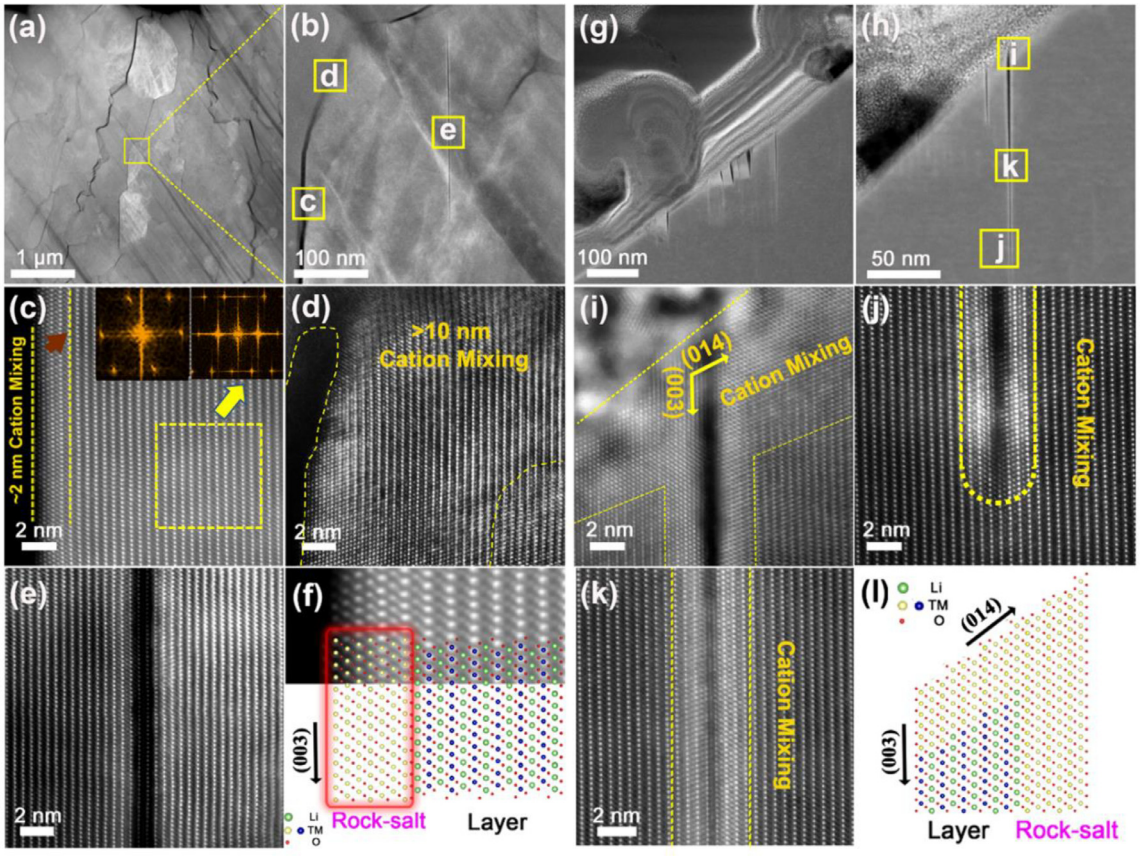

Fig. 4. HAADF-STEM images of the cross-sectioned, cycled N83 aggregates and S83 particles after 30 cycles between 2.8–4.5 V. (a, b) Low magnification HAADF images from the cycled N83 aggregates. Atomic-resolution HAADF images taken from the well detached part (c) and the crack tip (d) of an intergranular crack, and the intragranular crack within the primary particle (e). Atomic structure of (003) surface of Layered@Rocksalt structures (f). (g, h) Low magnification HAADF images from the cycled S83 particle. Atomic-resolution HAADF images taken from the surface part (i), the crack tip (j) and well detached part (k) of the intragranular crack. (e) and (l) show the crystallographic models of (010) and ($\bar{1}$04) surface geometry of Layered@Rocksalt structures.

cycled N83 and S83 materials. We first check the atomic structure of the surface and cracks of polycrystalline N83 material. As shown in Fig. 4a-b, in addition to the widespread intergranular cracks, intragranular cracks also exist within a cycled N83 primary particle. Atomic-resolution HAADF images taken from the well detached part (Fig. 4c) and the crack tip (Fig. 4d) of an intergranular crack indicate rather different surface structures. The well detached part exposes a (001) polar surface with a 2 nm-thick cation mixing layer (Fig. 4c), whereas the crack tip demonstrates a partly detached surface with much thicker (>10 nm) cation mixing

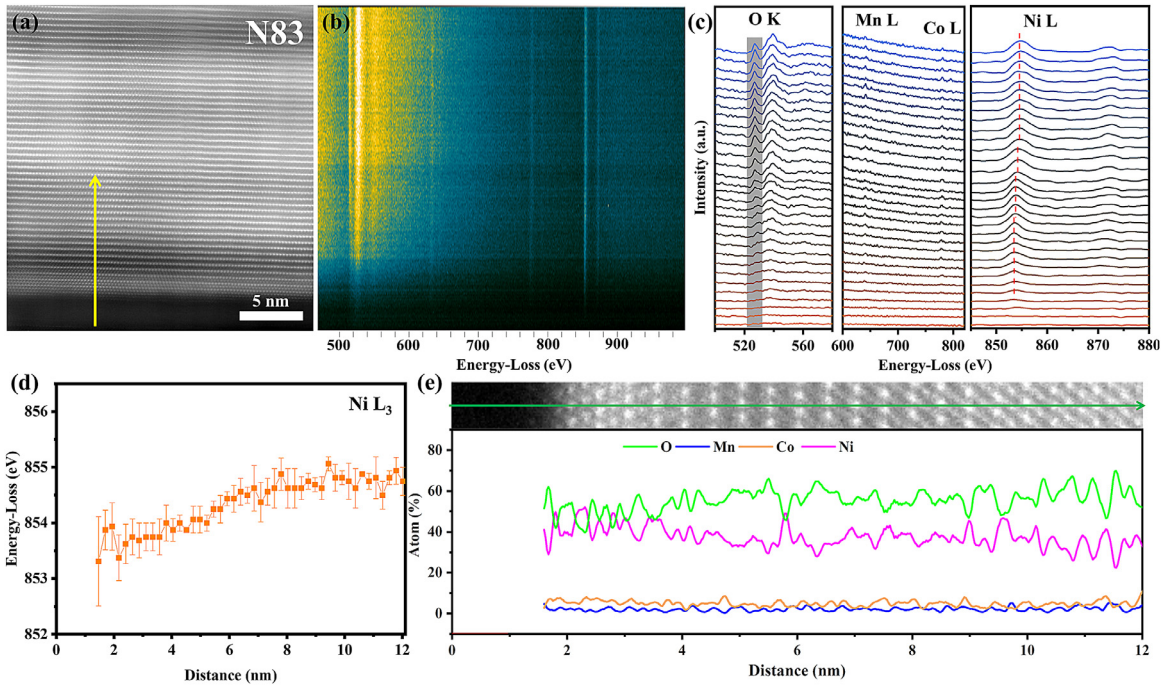

Fig. 5. Atomic resolution EELS and EDS line-scan analyses across the cracks of the N83 material after 100 cycles between 2.8–4.5 V. EELS spectrum image (b) from the vertical yellow line in the STEM image of the well detached crack of the N83 particle (a), showing O K, Mn, Co and Ni $L_{2,3}$ edges (c). (d) Corresponding energy profile of Ni L_3 edge from the surface to the interior. (e) EDS line-scan analyses across the crack, showing O, Mn, Co and Ni concentrations. (For interpretation of the references to color in this figure legend, the reader is referred to the web version of this article.)

layer (Fig. 4d). The corresponding fast Fourier transform (FFT) patterns confirm that these cation mixing layers possess a rocksalt-like structure, as illustrated schematically in Fig. 4f [33–35]. As for the intragranular crack within the primary particle, interlayer cleavage along (00l) crystallographic plane is evident, but no apparent cation mixing can be detected near the crack (Fig. 4e).

We now turn to the atomic structure of the cycled S83 material. It can be seen that large intragranular cracks open up on the surface and inside the grain (Fig. 4g-h). The cracks either on the surface or inside the bulk are located on the (00l) crystallographic plane, which is the same with the intragranular cracks of polycrystalline N83 material. Atomic-resolution HAADF images taken from the surface part (Fig. 4i), the crack tip (Fig. 4j and S5) and well detached part (Fig. 4k) of the intragranular cracks confirm the existence of thick cation-mixing layer on the $(\bar{1}04)$ nonpolar surface, thin cation-mixing layer on the (001) polar surface (see the crystallographic model in Fig. 4l) and a cation-mixing zone near the crack tips.

The composition and chemical evolution along the inter- and intra-granular cracks were studied in details through EELS line-scans (Figs. 5a-d and 6a-d). It is detected that the reduced O pre-peak intensities are associated with the cation-mixing layers in both the cycled N83 and S83 materials [36,37], as shown in the gray shaded rectangles in Figs. 5c and 6c. The relative distribution of chemical composition (Fig. S6) shows the content of O on average is ~55% in the first ~5 nm surface layer compared with the bulk value of ~65%. According to the valence state of TM ions and the composition ratio between TM and O ions, the relative amount of rocksalt TMO and layered NLO phases are estimated to be about 2/3 and 1/3, respectively, confirming the occurrence of surface reconstruction and formation of rocksalt-like phases detected by atomic-resolution characterization (Fig. 4). In addition, the Mn- and Co- L-edge white lines in the cation-mixing layers (Figs. 5c and 6c), compared with those for the bulk in both polycrystalline and single-crystal materials, show negligible changes in energy, whereas the Ni L_3 white lines exhibit a noticeable shift to lower energies, as plotted in Figs. 5d and 6d. That suggests the surface segregation of Ni cations to the crack surface and the formation of NiO-like phase in the cation-mixing layers (Figs. 5e and 6e).

The EDS line-scan result in Fig. 6e also displays Mn, Co enrichments in the crevice, demonstrating the preferential dissolution of Mn and Co from the bulk. It should be noted that the crevice in the primary particle of polycrystalline N83 does not show detectable surface reconstruction and TM dissolution. This preferential dissolution of Mn and Co was further confirmed by the corresponding ICP-OES results (Fig. S7). The TM concentration in the electrolyte obtained by ICP-OES is Ni:Co:Mn = 59:17:24 and 66:16:18 for N83 and S83, respectively, which deviates from the nominal composition in the pristine materials that Ni:Co:Mn = 83:10:7. The preferential dissolution of Mn and Co is more serious in the polycrystalline N83 material, when compared with the single-crystal S83 material, which is probably related to the different exposed surface indexes in these two materials [38].

3.3. Mechanism of stress-corrosion cracking

On the basis of above experimental results and our previous theoretical study [38], a surface-dependent mechanical-electrochemical coupling mechanism is proposed to interpret the cracking behaviors in the NLO polycrystalline aggregates and single crystals. In previous study, we have found the NLO particles show a strong elastic anisotropy during cycling. Among these common low-index surfaces, the (001) surface shows the maximum differences in the Young's moduli during charge-discharge process. The sharp decrease of Young's moduli along [001] at charge process causes the preferential tensile deformation along [001]. Besides, nonpolar surfaces such as (100), (110) and (104) has been found to suffer from severe Ni segregation, which facilitates the phase transformation from layered to rocksalt structure, as evidenced from [39].

In this work, both the intergranular and intragranular cracks tend to initiate and propagate via interlayer cleavage along (001)

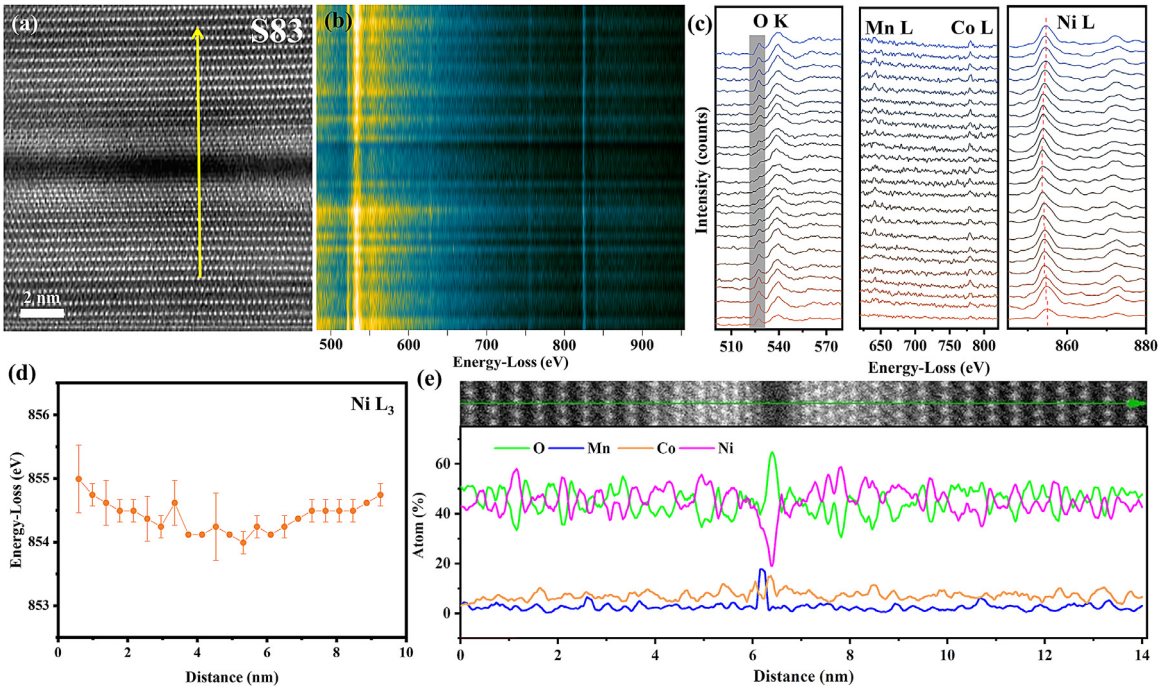

Fig. 6. Atomic resolution EELS and EDS line-scan analyses across the cracks of the S83 material after 100 cycles between 2.8–4.5 V. EELS spectrum image (b) from the vertical yellow line in the STEM image of the well detached crack of the S83 particle (a), showing O K, Mn, Co and Ni $L_{2,3}$ edges (c). (d) Corresponding energy profile of Ni $L_{2,3}$ edge from the surface to the interior. (e) EDS line-scan analyses across the crack, showing O, Mn, Co and Ni concentrations.

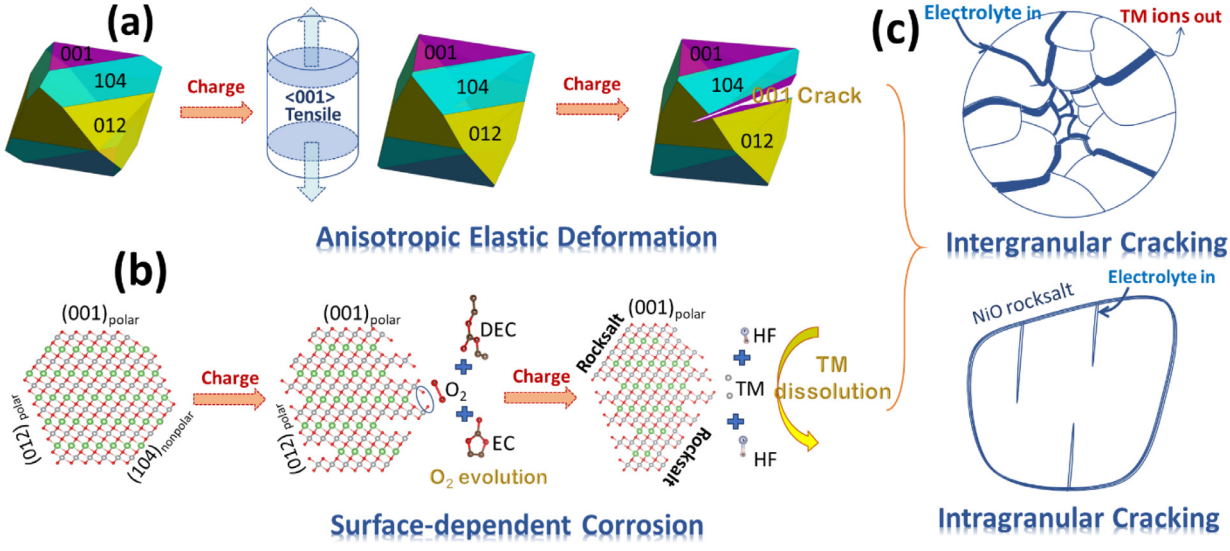

Fig. 7. Schematic illustration of the surface-dependent stress corrosion mechanism. (a) Anisotropic elastic deformation along [001] crystallographic orientation of primary particle. (b) Surface-dependent corrosion (oxygen evolution and TM dissolution) during cycling. (c) Resultant cracking models of polycrystalline and single-crystal NLOs.

basal plane. Surface reconstruction occurs on the fresh surfaces along the crack, when exposed to liquid electrolyte. A cation-mixing nanolayer which forms during surface reconstruction further accelerates the crack propagation by preventing the recovery of crack in following cycles. The preferential crack initiation along (001) basal plane could be correlated to surface orientation-dependent elastic anisotropy during electrochemical cycling, as well discussed in our previous theoretical study [38]. As shown in Fig. 7a, based on the data in our previous work [38], the primary particle synthesized at 850 °C and oxygen atmosphere was simulated. The particle is mainly composed of polar (001), polar (012) and nonpolar (104) surfaces. The large elastic anisotropy of (001) surface brings about uneven tensile deformation along [001] direction during electrochemical cycling. That leads to preferential (001) interlayer cleavage or crack initiation not only at (001)-terminated grain boundary (Fig. 4c), but also from the interior of primary particle (Fig. 4e-f) in polycrystalline aggregates and a single crystal particle (Fig. 4g-k).

In addition to the tensile deformation, we turn to taking a look at the cracking behaviors of NLOs from a corrosion perspective. The NLOs are known to have layered-to-spinel or layered-to-rocksalt transformations, especially on the surface, which are accompanied by a certain amount of oxygen gas release [40]. The transformations are also promoted by the exothermic (combustion in extreme

cases) reactions with the organic solutions (EC, DMC, EMC, etc) [41]. Using EC as a typical example, the cathode-electrolyte reactions are:

$$Li_{0.5}TMO_2 + 1/15\ C_3H_4O_3 \rightarrow 1/2\ LiTMO_2 + 1/6\ TM_3O_4 + 1/5\ CO_2 + 2/15\ H_2O \quad (1)$$

$$Li_{0.5}TMO_2 + 1/10\ C_3H_4O_3 \rightarrow 1/2\ LiTMO_2 + 1/2\ TMO + 3/10\ CO_2 + 1/5\ H_2O \quad (2)$$

for layered-to-spinel and layered-to-rocksalt transformations, respectively. The reaction enthalpies (ΔH) were calculated to be -0.7301 eV (-63.1455 kJ mol^{-1}) and -0.9927 eV (-95.7806 kJ mol^{-1}) for reaction (1) and (2), respectively. The corresponding surface atomic structure evolution in primary particle with various exposed surfaces was illustrated in Fig. 7b. The delithiated nonpolar (104) surface has dangling TM-O bonds which will easily promote the layered-to-rocksalt transformation and oxygen evolution. We would expect the nonpolar (104) surface of NLOs after delithiation will consist of defected layered $LiTMO_2$ and rocksalt TMO phases (see Fig. 4). The exothermic nature of layered-to-rocksalt phase transformation also provides the energy and water (H_2O) needed for the decomposition of $LiPF_6$ salt (~84.27 kJ mol^{-1} at 298 K) [42]:

$$LiPF_6 + H_2O \rightarrow LiF + POF_3 + 2HF \quad (3)$$

The decomposition of $LiPF_6$ gives rise to hydrofluoric acid (HF), further corroding the surface layer of NLOs [43]. After a throughout screening of all possible reactions, the most energetically favorable reaction between the surface layer of delithiated NLOs and HF are as follows:

$$LiNiO_2 + NiO + 6\ HF \rightarrow LiF + NiF_3 + NiF_2 + 3\ H_2O \quad (4)$$

$$LiCoO_2 + CoO + 6\ HF \rightarrow LiCoF_4 + CoF_2 + 3\ H_2O \quad (5)$$

$$LiMnO_2 + MnO + 6\ HF \rightarrow LiMnF_4 + MnF_2 + 3\ H_2O \quad (6)$$

The reaction enthalpies (ΔH) of reaction (4), (5), and (6) are -3.370 eV (-325 kJ mol^{-1}), -3.998 eV (-386 kJ mol^{-1}), and -5.168 eV (-499 kJ mol^{-1}), respectively. According to the reaction enthalpies, the above HF attack reactions are energetically favorable, and the likelihood of TM dissolution follows Mn > Co >Ni. It should be noted the actual reaction rate are depended on the reaction sites on the surface, that is Ni > Co > Mn. That means Ni will dissolve more into the electrolyte even though the reaction enthalpy is the highest among three TM species. Nevertheless, in view of the whole TM dissolution process, the Mn and Co ions on the surface dissolve relatively more into the electrolyte, which will leave Ni at the surface of the delithiated NLOs. This is in qualitatively agreement with the experimental observation (Figs. 4–6) that the preferential dissolution of Mn and Co into electrolyte detected by the ICP-OES, and the rocksalt NiO on the surface of NLOs by HADDF-STEM and EELS. It should be noted that these reactions (4)-(6) produced more H_2O which will further react with $LiPF_6$ and produce more HF leading to repeated surface corrosion reaction cycles of metal loss.

According to above analyses, a universal chain stress-corrosion mechanism can be summarized for the degradation of NLOs, which is surface orientation sensitive. Firstly, the strong anisotropy (001) tensile deformation at the higher voltages (or larger degree of charge (DOC), 75% of theoretical capacity for most NLOs) not only initiates the crack on (001) surface, but also creates fresh nonpolar surface as the crack opens up. Secondly, the fresh nonpolar surfaces, such as (100), (110), and (104), undergo a surface reconstruction transition from layered to rocksalt structure assisted by the combustion reactions with organic solutions (EC, DMC, EMC, etc.). Thirdly, this surface reconstruction reaction provides the necessities, heat and water, for the decomposition of $LiPF_6$ into HF and POF_3. Lastly, the HF attacks the surface rocksalt and layered structure, resulting in the TM dissolution and erosion of NLO particles. This chain stress corrosion repeats during each charge/discharge cycle, resulting in larger and larger cracks and smaller and smaller particles. The chain stress corrosion leads to completely disconnected primary particles within the polycrystalline aggregates and a thick and heterogeneous SEI layer on anode as a result of TM dissolution, which contributes to the capacity fading of the battery.[44–46]

3.4. Grain boundary engineering

The newly proposed stress-corrosion mechanism indicates an intrinsic trade-off between the polycrystalline and single crystal particles. In polycrystalline NLOs, even though they facilitate the fast diffusion of Li ions and high electrical conductivity, the weakly bonded grain boundaries detach as a result of anisotropic tensile stress during cycling. The fresh nonpolar surfaces undergo a surface reconstruction transition, and later dissolve into the electrolyte under HF attack. The large amount of grain boundaries and deficient primary particle surface result in more severer stress corrosion in the center of polycrystalline aggregates, as evident in cross-section SEM (Fig. 3) in this work and in the literature [4–8]. On the other hand, single-crystal NLOs which have preexisting surface reconstruction layer on the particle and sluggish kinetics deliver a lower capacity at the same voltage compared with the polycrystalline counterparts [24]. In this case, the anisotropic tensile deformation is less significant and accordingly the surface reconstruction reaction is alleviated. However, at higher voltages or larger DOC, the crack initiates and propagates and the same stress corrosion reaction develops from the surface into the bulk. It should be noted that the surface reconstruction layer of single-crystal particle due to higher annealing temperatures could partly inhibit the stress corrosion by eliminating the production of water during the surface reconstruction from layered to rocksalt structure and thus preventing the decomposition of $LiPF_6$ and the following HF attack.

The stress corrosion mechanism and the trade-off of polycrystalline and single-crystal NLOs entail a grain boundary engineering strategy in the design of high-performance NLOs. The rationale is to design a particle structure which could preserve the nonpolar grain boundary for the fast Li diffusion in the meantime reduce the anisotropic (001) tensile deformation and the subsequent stress corrosion. Recently, radially oriented primary nanosheets and nanorods were realized in polycrystalline $LiNi_{0.8}Co_{0.1}Mn_{0.1}O_2$[47], $LiNi_xCo_yB_{1-x-y}O_2$[48], and $LiNi_{0.9}Co_{0.09}W_{0.01}O_2$[49], respectively. The synthesized spherical secondary particle is composed of primary particles with their [001] axis along the radial direction of spherical secondary particle, which enables even radically expansion and shrinkage of the spherical primary particle during cycling. Nevertheless, crack still presents after extended charge/discharge cycles, as the grain boundary is composed of weakly bonded (100) surface [48, 49]. In view of these results, a better grain boundary design would be keeping the radially [001] arrangement in primary particle to accommodate the anisotropic (001) tensile deformation, but connecting each primary particle with stronger grain boundary through the more stable (104) surface. Alternatively, the secondary particle could be formed by interlocking few micron-size single-crystal primary particle to prevent the TM dissolution and enable faster Li diffusion.

4. Conclusions

In summary, combining electrochemical analyses, electron microscopy and spectroscopy observations, and theoretical calculations, we demonstrate that both the intergranular and intragranular cracks initiate and propagate along polar (001) basal plane and surface structure transition and TM dissolution occur preferentially on nonpolar surfaces such as (104) plane, due to surface-dependent stress-corrosion coupling effects. In the crack surface of NLOs, the layered structure turns into rock-salt structure along with cation mixing, and Ni cations gather on the near surface (~5 nm) and Co, Mn cations aggregate at the crack area. Severe intergranular cracking that accumulates within the polycrystalline NLO aggregates accounts mostly for the fast voltage decay and capacity fading, whereas minor intragranular cracking and less surface damage lead to substantial improvements on cyclability and reversible capacity of single-crystal NLOs. To optimize the specific capacity and cycling stability, proper grain boundary engineering strategies may further improve the performance of NLO cathode materials for advanced batteries.

Declaration of Competing Interest

The authors declare that they have no known competing financial interests or personal relationships that could have appeared to influence the work reported in this paper.

Acknowledgements

The authors would like to acknowledge financial support from National Natural Science Foundation of China (51971250), the National Key Research and Development Program of China (Grant No. 2018YFB010400), the State Key Laboratory of Powder Metallurgy at Central South University. P. Gao gratefully acknowledges the support from the National Program for Thousand Young Talents of China, the Key R&D Program of Guangdong Province (2018B030327001, 2018B010109009), and "2011 Program" Peking-Tsinghua-IOP Collaborative Innovation Center of Quantum Matter. Z.-P. Ding acknowledges the support from China Postdoctoral Science Foundation (2019M650333).

Supplementary materials

Supplementary material associated with this article can be found, in the online version, at doi:10.1016/j.actamat.2021.116914.

References

[1] J. Kim, H. Lee, H. Cha, M. Yoon, M. Park, J. Cho, Prospect and reality of Ni-rich cathode for commercialization, Adv. Energy Mater. 8 (2018) 1–25, doi:10.1002/aenm.201702028.
[2] W. Li, B. Song, A. Manthiram, High-voltage positive electrode materials for lithium-ion batteries, Chem. Soc. Rev. 46 (2017) 3006–3059, doi:10.1039/C6CS00875E.
[3] E.M. Erickson, F. Schipper, T.R. Penki, J.-Y. Shin, C. Erk, F.-F. Chesneau, B. Markovsky, D. Aurbach, Review—recent advances and remaining challenges for lithium ion battery cathodes, J. Electrochem. Soc. 164 (2017) A6341–A6348.
[4] H. Liu, M. Wolf, K. Karki, Y.-S. Yu, E.A. Stach, J. Cabana, K.W. Chapman, P.J. Chupas, Intergranular cracking as a major cause of long-term capacity fading of layered cathodes, Nano Lett 17 (2017) 3452–3457, doi:10.1021/acs.nanolett.7b00379.
[5] E.-J. Lee, Z. Chen, H.-J. Noh, S.C. Nam, S. Kang, D.H. Kim, K. Amine, Y.-K. Sun, Development of microstrain in aged lithium transition metal oxides, Nano Lett. 14 (2014) 4873–4880, doi:10.1021/nl5022859.
[6] A.O. Kondrakov, A. Schmidt, J. Xu, H. Gesswein, R. Monig, P. Hartmann, H. Sommer, T. Brezesinski, J. Janek, Anisotropic lattice strain and mechanical degradation of high- and low-nickel NCM cathode materials for Li-ion batteries, J. Phys. Chem. C 121 (2017) 3286–3294, doi:10.1021/acs.jpcc.6b12885.
[7] P. Yan, J. Zheng, M. Gu, J. Xiao, J.-G. Zhang, C.-M. Wang, Intragranular cracking as a critical barrier for high-voltage usage of layer-structured cathode for lithium-ion batteries, Nat. Commun. 8 (2017) 14101, doi:10.1038/ncomms14101.
[8] J.-M. Lim, T. Hwang, D. Kim, M.-S. Park, K. Cho, M. Cho, Intrinsic origins of crack generation in Ni-rich $LiNi_{0.8}Co_{0.1}Mn_{0.1}O_2$ layered oxide cathode material, Sci. Rep. 7 (2017) 39669, doi:10.1038/srep39669.
[9] A. Mukhopadhyay, B.W. Sheldon, Deformation and stress in electrode materials for Li-ion batteries, Prog. Mater. Sci. 63 (2014) 58–116, doi:10.1016/j.pmatsci.2014.02.001.
[10] Z. Yu, S.-L. Shang, M.L. Gordin, A. Mousharraf, Z.K. Liu, D. Wang, Ti-substituted $Li[Li_{0.26}Mn_{0.6-x}Ti_xNi_{0.07}Co_{0.07}]O_2$ layered cathode material with improved structural stability and suppressed voltage fading, J. Mater. Chem. A 3 (2015) 17376–17384.
[11] T.E. Conry, A. Mehta, J. Cabana, M.M. Doeff, Structural underpinnings of the enhanced cycling stability upon Al-substitution in $LiNi_{0.45}Mn_{0.45}Co_{0.1-y}Al_yO_2$ positive electrode materials for Li-ion batteries, Chem. Mater. 24 (2012) 3307–3317, doi:10.1021/cm3011937.
[12] K. Tatsumi, Y. Sasano, S. Muto, T. Yoshida, T. Sasaki, K. Horibuchi, Y. Takeuchi, Y. Ukyo, Local atomic and electronic structures around Mg and Al dopants in $LiNiO_2$ electrodes studied by XANES and ELNES and first-principles calculations, Phys. Rev. B 78 (2008) 045108, doi:10.1103/PhysRevB.78.045108.
[13] Y.-K. Sun, S.-T. Myung, B.-C. Park, J. Prakash, I. Belharouak, K. Amine, High-energy cathode material for long-life and safe lithium batteries, Nat. Mater. 8 (2009) 320–324, doi:10.1038/nmat2418.
[14] Y.-K. Sun, S.-T. Myung, M.-H. Kim, J. Prakash, K. Amine, Synthesis and characterization of $Li[(Ni_{0.8}Co_{0.1}Mn_{0.1})_{0.8}(Ni_{0.5}Mn_{0.5})_{0.2}]O_2$ with the microscale core−shell structure as the positive electrode material for lithium batteries, J. Am. Chem. Soc. 127 (2005) 13411–13418, doi:10.1021/ja053675g.
[15] Y. Cho, P. Oh, J. Cho, A new type of protective surface layer for high-capacity Ni-based cathode materials: nanoscaled surface pillaring layer, Nano Lett. 13 (2013) 1145–1152, doi:10.1021/nl304558t.
[16] F. Lin, D. Nordlund, Y. Li, M.K. Quan, L. Cheng, T.C. Weng, Y. Liu, H.L. Xin, M.M. Doeff, Metal segregation in hierarchically structured cathode materials for high-energy lithium batteries, Nat. Energy 1 (2016) 1–8, doi:10.1038/nenergy.2015.4.
[17] Y.-K. Sun, Z. Chen, H.-J. Noh, D.-J. Lee, H.-G. Jung, Y. Ren, S. Wang, C.S. Yoon, S.-T. Myung, K. Amine, Nanostructured high-energy cathode materials for advanced lithium batteries, Nat. Mater. 11 (2012) 942–947, doi:10.1038/nmat3435.
[18] H.-J. Noh, S. Youn, C.S. Yoon, Y.-K. Sun, Comparison of the structural and electrochemical properties of layered $Li[Ni_xCo_yMn_z]O_2$ (x = 1/3, 0.5, 0.6, 0.7, 0.8 and 0.85) cathode material for lithium-ion batteries, J. Power Sources 233 (2013) 121–130, doi:10.1016/j.jpowsour.2013.01.063.
[19] X. Fan, G. Hu, B. Zhang, X. Ou, J. Zhang, W. Zhao, H. Jia, L. Zou, P. Li, Y. Yang, Crack-free single-crystalline Ni-rich layered NCM cathode enable superior cycling performance of lithium-ion batteries, Nano Energy 70 (2020) 104450, doi:10.1016/j.nanoen.2020.104450.
[20] J. Zhu, G. Chen, Single-crystal based studies for correlating the properties and high-voltage performance of $Li[Ni_xMn_yCo_{1-x-y}]O_2$ cathodes, J. Mater. Chem. A 7 (2019) 5463–5474, doi:10.1039/c8ta10329a.
[21] Z. Zhao, B. Huang, M. Wang, X. Yang, Y. Gu, Facile synthesis of fluorine doped single crystal Ni-rich cathode material for lithium-ion batteries, Solid State Ionics 342 (2019) 115065, doi:10.1016/j.ssi.2019.115065.
[22] J.E. Harlow, X. Ma, J. Li, E. Logan, Y. Liu, N. Zhang, L. Ma, S.L. Glazier, M.M.E. Cormier, M. Genovese, S. Buteau, A. Cameron, J.E. Stark, J.R. Dahn, A wide range of testing results on an excellent lithium-ion cell chemistry to be used as benchmarks for new battery technologies, J. Electrochem. Soc. 166 (2019) A3031–A3044, doi:10.1149/2.0981913jes.
[23] F. Zhang, S. Lou, S. Li, Z. Yu, Q. Liu, A. Dai, C. Cao, M.F. Toney, M. Ge, X. Xiao, W.K. Lee, Y. Yao, J. Deng, T. Liu, Y. Tang, G. Yin, J. Lu, D. Su, J. Wang, Surface regulation enables high stability of single-crystal lithium-ion cathodes at high voltage, Nat. Commun. 11 (2020), doi:10.1038/s41467-020-16824-2.
[24] C. Xu, K. Märker, J. Lee, A. Mahadevegowda, P.J. Reeves, S.J. Day, M.F. Groh, S.P. Emge, C. Ducati, B.Layla Mehdi, C.C. Tang, C.P. Grey, Bulk fatigue induced by surface reconstruction in layered Ni-rich cathodes for Li-ion batteries, Nat. Mater. 20 (2021) 84–92, doi:10.1038/s41563-020-0767-8.
[25] B.H. Toby, EXPGUI, a graphical user interface for GSAS, J. Appl. Crystallogr. 34 (2001) 210–213, doi:10.1107/S0021889801002242.
[26] C. Liang, R.C. Longo, F. Kong, C. Zhang, Y. Nie, Y. Zheng, J.-S. Kim, S. Jeon, S. Choi, K. Cho, Obstacles toward unity efficiency of $LiNi_{1-2x}Co_xMn_xO_2$ (x = 0 ~ 1/3) (NCM) cathode materials: Insights from ab initio calculations, J. Power Sources. 340 (2017), doi:10.1016/j.jpowsour.2016.11.056.
[27] A. Jain, S.P. Ong, G. Hautier, W. Chen, W.D. Richards, S. Dacek, S. Cholia, D. Gunter, D. Skinner, G. Ceder, K.A. Persson, Commentary: the materials project: a materials genome approach to accelerating materials innovation, APL Mater. 1 (2013) 011002, doi:10.1063/1.4812323.
[28] C. Fu, G. Li, D. Luo, Q. Li, J. Fan, L. Li, Nickel-rich layered microspheres cathodes: lithium/nickel disordering and electrochemical performance, ACS Appl. Mater. Interfaces 6 (2014) 15822–15831, doi:10.1021/am5030726.
[29] F. Wu, N. Liu, L. Chen, Y. Su, G. Tan, L. Bao, Q. Zhang, Y. Lu, J. Wang, S. Chen, J. Tan, Improving the reversibility of the H2-H3 phase transitions for layered Ni-rich oxide cathode towards retarded structural transition and enhanced cycle stability, Nano Energy 59 (2019) 50–57, doi:10.1016/j.nanoen.2019.02.027.
[30] J.A. Gilbert, J. Bareno, T. Spila, S.E. Trask, D.J. Miller, B.J. Polzin, A.N. Jansen, D.P. Abraham, Cycling behavior of NCM523/graphite lithium-ion cells in the 3-4.4 V range: diagnostic studies of full cells and harvested electrodes, J. Electrochem. Soc. 164 (2017) A6054–A6065, doi:10.1149/2.0081701jes.

[31] B.S. Kumar, A. Pradeep, A. Dutta, A. Mukhopadhyay, Water-stable O_3-type layered Na transition metal oxides enabling environment friendly 'aqueous processing' of electrodes with long-term electrochemical stability, J. Mater. Chem. A 8 (2020) 18064–18078, doi:10.1039/D0TA05169A.
[32] R. Jung, M. Metzger, F. Maglia, C. Stinner, H.A. Gasteiger, Oxygen release and its effect on the cycling stability of $LiNi_xMn_yCo_zO_2$ (NMC) cathode materials for Li-ion batteries, J. Electrochem. Soc. 164 (2017) A1361–A1377, doi:10.1149/2.0021707jes.
[33] S. Hwang, S.M. Kim, S.M. Bak, B.W. Cho, K.Y. Chung, J.Y. Lee, W. Chang, E.A. Stach, Investigating local degradation and thermal stability of charged nickel-based cathode materials through real-time electron microscopy, ACS Appl. Mater. Interfaces 6 (2014) 15140–15147, doi:10.1021/am503278f.
[34] D. Zeng, J. Cabana, J. Bréger, W.-S. Yoon, C.P. Grey, Cation ordering in $Li[Ni_xMn_xCo_{(1-2x)}]O_2$ -layered cathode materials: a nuclear magnetic resonance (NMR), pair distribution function, X-ray absorption spectroscopy, and electrochemical study, Chem. Mater. 19 (2007) 6277–6289, doi:10.1021/cm702241a.
[35] H.-H. Sun, A. Manthiram, Impact of microcrack generation and surface degradation on a nickel-rich layered $Li[Ni_{0.9}Co_{0.05}Mn_{0.05}]O_2$ cathode for lithium-ion BATTERies, Chem. Mater. 29 (2017) 8486–8493, doi:10.1021/acs.chemmater.7b03268.
[36] B. Qiu, M. Zhang, L. Wu, J. Wang, Y. Xia, D. Qian, H. Liu, S. Hy, Y. Chen, K. An, Y. Zhu, Z. Liu, Y.S. Meng, Gas–solid interfacial modification of oxygen activity in layered oxide cathodes for lithium-ion batteries, Nat. Commun. 7 (2016) 12108, doi:10.1038/ncomms12108.
[37] K. Kubota, T. Kaneko, M. Hirayama, M. Yonemura, Y. Imanari, K. Nakane, R. Kanno, Direct synthesis of oxygen-deficient Li_2MnO_{3-x} for high capacity lithium battery electrodes, J. Power Sources 216 (2012) 249–255, doi:10.1016/j.jpowsour.2012.05.061.
[38] C. Liang, R.C. Longo, F. Kong, C. Zhang, Y. Nie, Y. Zheng, K. Cho, Ab initio study on surface segregation and anisotropy of Ni-rich $LiNi_{1-2y}Co_yMn_yO_2$ (NCM) (y </= 0.1) Cathodes, ACS Appl. Mater. Interfaces 10 (2018) 6673–6680, doi:10.1021/acsami.7b17424.
[39] F. Lin, I.M. Markus, D. Nordlund, T.-C. Weng, M.D. Asta, H.L. Xin, M.M. Doeff, Surface reconstruction and chemical evolution of stoichiometric layered cathode materials for lithium-ion batteries, Nat. Commun. 5 (2014) 3529, doi:10.1038/ncomms4529.
[40] S. Hwang, S.M. Kim, S.M. Bak, S.Y. Kim, B.W. Cho, K.Y. Chung, J.Y. Lee, E.A. Stach, W. Chang, Using real-time electron microscopy to explore the effects of transition-metal composition on the local thermal stability in charged $Li_xNi_yMn_zCo_{1-y-z}O_2$ cathode materials, Chem. Mater. 27 (2015) 3927–3935, doi:10.1021/acs.chemmater.5b00709.
[41] L. Wang, T. Maxisch, G. Ceder, A first-principles approach to studying the thermal stability of oxide cathode materials, Chem. Mater. 19 (2007) 543–552, doi:10.1021/cm0620943.
[42] H. Yang, G.V. Zhuang, P.N. Ross, Thermal stability of LiPF6 salt and Li-ion battery electrolytes containing LiPF6, J. Power Sources 161 (2006) 573–579, doi:10.1016/j.jpowsour.2006.03.058.
[43] M. Aykol, S. Kirklin, C. Wolverton, Thermodynamic aspects of cathode coatings for lithium-ion batteries, Adv. Energy Mater. 4 (2014) 1400690, doi:10.1002/aenm.201400690.
[44] W. Li, A. Dolocan, P. Oh, H. Celio, S. Park, J. Cho, A. Manthiram, Dynamic behaviour of interphases and its implication on high-energy-density cathode materials in lithium-ion batteries, Nat. Commun. 8 (2017), doi:10.1038/ncomms14589.
[45] W. Li, U.-H. Kim, A. Dolocan, Y.-K. Sun, A. Manthiram, Formation and inhibition of metallic lithium microstructures in lithium batteries driven by chemical crossover, ACS Nano 11 (2017) 5853–5863, doi:10.1021/acsnano.7b01494.
[46] J. Kim, H. Ma, H. Cha, H. Lee, J. Sung, M. Seo, P. Oh, M. Park, J. Cho, A highly stabilized nickel-rich cathode material by nanoscale epitaxy control for high-energy lithium-ion batteries, Energy Environ. Sci. 11 (2018) 1449–1459, doi:10.1039/c8ee00155c.
[47] X. Xu, H. Huo, J. Jian, L. Wang, H. Zhu, S. Xu, X. He, G. Yin, C. Du, X. Sun, Radially oriented single-crystal primary nanosheets enable ultrahigh rate and cycling properties of $LiNi_{0.8}Co_{0.1}Mn_{0.1}O_2$ cathode material for lithium-ion batteries, Adv. Energy Mater. 9 (2019) 1–9, doi:10.1002/aenm.201803963.
[48] H. Ryu, N. Park, D.R. Yoon, U. Kim, C.S. Yoon, Y. Sun, New class of Ni-rich cathode materials $Li[Ni_xCo_yB_{1-x-y}]O_2$ for next lithium batteries, Adv. Energy Mater. 10 (2020) 2000495, doi:10.1002/aenm.202000495.
[49] H.H. Ryu, K.J. Park, D.R. Yoon, A. Aishova, C.S. Yoon, Y.K. Sun, $Li[Ni_{0.9}Co_{0.09}W_{0.01}]O_2$: A new type of layered oxide cathode with high cycling stability, Adv. Energy Mater. 9 (2019) 0–6, doi:10.1002/aenm.201902698.